Dissipative edge transport in disordered axion insulator films

Zhaochen Liu,[1] Dongheng Qian,[1] Yadong Jiang,[1] and Jing Wang[1,2,3,*]

[1]*State Key Laboratory of Surface Physics and Department of Physics, Fudan University, Shanghai 200433, China*
[2]*Institute for Nanoelectronic Devices and Quantum Computing, Fudan University, Shanghai 200433, China*
[3]*Zhangjiang Fudan International Innovation Center, Fudan University, Shanghai 201210, China*

(Received 9 November 2021; revised 25 January 2022; accepted 21 November 2023; published 6 December 2023)

We investigate the role of disorder in the edge transport of axion insulator films. We predict by first-principles calculations that even-number-layer $MnBi_2Te_4$ have gapped helical edge states. The random potential will dramatically modify the edge spectral function to become *gapless*. However, such gapless helical state here is fundamentally different from that in the quantum spin Hall insulator or topological Anderson insulator. We further study the edge transport in this system by Landauer-Büttiker formalism, and find such gapless edge state is dissipative and not immune to backscattering, which would explain the dissipative nonlocal transport in the axion insulator state observed in six-septuple-layer $MnBi_2Te_4$ experimentally. Transport experiments with floating leads are proposed to verify our theory on the dissipative helical edge channels. In particular, the longitudinal resistance can be greatly reduced by adding an extra floating probe, even if it is not used. These results will facilitate the observation of the long-sought topological magnetoelectric effect in axion insulators.

DOI: 10.1103/PhysRevB.108.245116

I. INTRODUCTION

Topological phenomena have been one of the central topics in condensed matter physics [1–4]. The interplay between band topology and magnetism gives rise to a variety of exotic quantum states [4–6]. A prime example is the quantum anomalous Hall (QAH) effect with gapless chiral edge states discovered in magnetic topological insulator (TI) films [5,7–17]. Another interesting example is the axion insulator, which is a three-dimensional magnetic TI with a nonzero quantized Chern-Simons magnetoelectric coupling (axion $\theta = \pi$) protected by inversion symmetry $\mathcal{I}$ instead of time-reversal symmetry Θ [5,18–23]. Such axion coupling leads to the prediction of the topological magnetoelectric (TME) effect [5], which is the hallmark of an axion insulator, but remains unexplored due to difficulties in realizing the axion insulator state.

The simplest scenario for the axion insulator state is obtained in bulk TI with a surface gap induced by a hedgehog magnetization while preserving the bulk gap [5,24–26]. In the thin-film geometry, the above condition of hedgehog magnetization is simply fulfilled with an antiparallel magnetization on the top and bottom surfaces, where the absence of all surface state transport leads to a zero Hall plateau: $\rho_{xy} = 0$, $\rho_{xx} \to \infty$ and $\sigma_{xy} = 0$, $\sigma_{xx} \to 0$ [25,27]. Such peculiar charge transports have been observed in a ferromagnetic (FM)-TI-FM heterostructure [28–31] and even-layer $MnBi_2Te_4$ antiferromagnetic (AFM) TI [32], which were predicted to be an axion insulator state [25,33–38]. Theoretically, the low-energy physics in two different systems are similar and generate a topological θ response which is nonquantized due to the finite-size effect [25,26,39]. However, recent transport and microwave imaging experiments find quite different behaviors in these two systems, where gapless edge states do not exist in the former [28,40] but do exist in the latter [41,42]. In particular, the edge transport in the $MnBi_2Te_4$ even layer is shown to be dissipative [41]. Thus, it is important to trace where such dissipative gapless edge states come from and understand the origin of the discrepancy in these two systems, which is vital for realizing the long-sought TME effect.

Here we study the role of disorder in the edge transport of axion insulator films. By combining first-principles calculations and analytic models, we show that six septuple layers (SLs) of $MnBi_2Te_4$ studied in experiments [41,42] have gapped helical edge states. A random potential will modify the edge spectral function to become gapless. Such gapless edge state is dissipative and not immune to backscattering, which would explain the dissipative transport of the recent transport and image experiments [41,42].

II. MODELS

A. Materials

We carry out first-principles calculations on $MnBi_2Te_4$ films. The material consists of van der Waals coupled SLs and develops A-type AFM order with an out-of-plane easy axis below the Néel temperature, which is ferromagnetic (FM) within each SL, but AFM between adjacent SLs along the z axis. The bulk state is an AFM TI with nontrivial Z_2 index protected by $S = \Theta\tau_{1/2}$ [43], where $\tau_{1/2}$ is the half translation operator along the z axis. The odd SL breaks $\mathcal{I}\Theta$ and shows the QAH effect [14,33–35], while the even SL with full compensated magnetic layers conserves $\mathcal{I}\Theta$ and exhibits zero-plateau QAH [32]. We study the edge band structure of the even SL along

*wjingphys@fudan.edu.cn

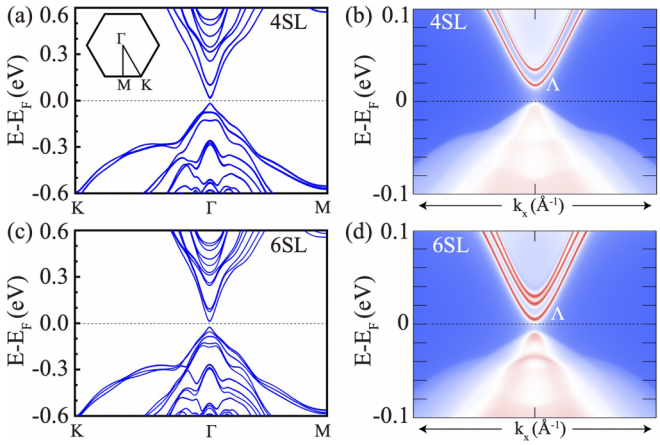

FIG. 1. (a),(c) Band structure for four-SL and six-SL $MnBi_2Te_4$. The dashed line indicates the Fermi level. The inset of (a) shows the two-dimensional (2D) Brillouin zone, with high-symmetry $\mathbf{k}$ points $\Gamma(0,0)$, $K(\pi,\pi)$, and $M(\pi,0)$ labeled. The energy dispersion of the semi-infinite film along edge ΓM is plotted for (b) four SL and (d) six SL, respectively. The *gapped* edge states are clearly seen around the Γ point as red lines dispersing in the 2D bulk gap.

the edge ΓM direction. The 2D band structure in Fig. 1 has an inverted band gap at the Γ point, and there indeed exists *gapped* helical edge state Λ in the insulating bulk. We notice that the lower branch of the gapped edge state is covered by the bulk valence bands. As we show below, it originates from helical edge states of the quantum spin Hall (QSH) effect, but with Θ-breaking due to magnetic ordering, where the gap is opened at the Dirac point.

B. Effective model

The effective model for the low-energy physics of the even SL can be written near the Γ point. We start from 3D Hamiltonian $H_{3d}(\mathbf{k})$ for AFM $MnBi_2Te_4$, which is the same as that for Θ-invariant TI due to conserved $\mathcal{S}$ [33]. For the even SL, $\mathcal{S}$ is broken and a term H_{ex} describing the spatial alternating exchange field enters into $H_{3d}(\mathbf{k})$. The confinement in the z direction quantizes k_z and leads to 2D subbands labeled by the subband index n. The 2D subbands have band inversion for film thickness $\geqslant 4$ SLs [33] and, without H_{ex}, the system is QSH with the low-energy physics determined by Dirac surface states on the top and bottom surfaces [44,45]. The effect of H_{ex} is to introduce opposite Zeeman terms on these two surfaces. Thus the effective model for the even SL described by the massive Dirac surface states is given by [25,46,47]

$$\mathcal{H}_0(\mathbf{k}) = \epsilon_0(\mathbf{k}) + v(k_y\sigma_x - k_x\sigma_y)\tau_z + m(\mathbf{k})\tau_x + \Delta\sigma_z\tau_z, \quad (1)$$

with the basis of $|t\uparrow\rangle$, $|t\downarrow\rangle$, $|b\uparrow\rangle$, and $|b\downarrow\rangle$, where t, b denote the top and bottom surfaces and $\uparrow$, $\downarrow$ represent spin-up and -down states, respectively. The particle-hole asymmetry $\epsilon_0(\mathbf{k})$ is neglected for simplicity. σ_i and τ_i $(i = x, y, z)$ are Pauli matrices acting on the spin and layer, respectively. v is the Dirac velocity, $m(\mathbf{k}) = m_0 + m_1(k_x^2 + k_y^2)$ describes the tunneling effect between t and b surface states, and Δ is the exchange field along the z axis introduced by the opposite magnetic ordering on t and b.

Equation (1) correctly characterizes the gapped helical edge state shown in Fig. 1. The energy gap for 2D bulk is $2\sqrt{m_0^2 + \Delta^2}$ at the Γ point. If $\Delta = 0$, this model is similar to the Bernevig-Hughes-Zhang model for HgTe quantum wells [48] describing the QSH with $m_0 m_1 < 0$, where there exists a gapless helical edge state. Then, Δ further induces a gap to the edge state. By projecting the Hamiltonian given by Eq. (1) onto the edge states, the effective model for the 1D gapped helical edge state is obtained analytically as $H_{1d} = vk_x\varrho_z + \Delta\varrho_x$, where ϱ_i are Pauli matrices denoting pseudospin in the basis of the left- and right-moving states. The edge state gap 2Δ is less than that of 2D bulk, consistent with Fig. 1. It is worth mentioning that there also exist other gapped helical edge states with higher energy than Λ in the 2D bulk gap, as shown in Fig. 1(d), which are from the band inversion of extra 2D subbands with $n > 1$ in thick film, where n is the subband index (see Supplemental Material [49]). In the following, we investigate the edge transport determined by Λ in the presence of disorder. Taking six SLs for a concrete example, we fit the parameters $v = 3.2$ eV Å, $m_0 = -0.014$ eV, $m_1 = 9.4$ eV Å^2, and $\Delta_z = 5$ meV.

In general, the disorder will generate spatially random perturbations to the pure Hamiltonian $\mathcal{H}_0$. Specifically, the system mainly has random scalar potential $\mathcal{H}_U = U(\mathbf{r})$ induced by impurities in the materials. There also exists a random exchange field along the z axis induced by the inhomogeneous AFM ordering $\mathcal{H}_\Delta = \Delta(\mathbf{r})\sigma_z\tau_z$. Here we are interested in a system deep in AFM axion state and the fluctuation of $|\Delta(\mathbf{r})| < |\Delta|$, thus the random $\Delta(\mathbf{r})$ just renormalizes Δ to a reduced value in Eq. (1) and will not essentially affect the edge transport. Therefore, we only need to consider $\mathcal{H}_U$, which is nonuniform and random in space but constant in time.

III. ANALYSIS OF DISORDER

Now we will show that disorder will renormalize Eq. (1). We extract the renormalized topological mass m_0 and the renormalized exchange field Δ, from the self-energy Σ of the disorder-averaged effective medium. In numerical simulations, we discretize $\mathcal{H}_0(\mathbf{k})$ on a square lattice and take a random on-site disorder potential $U(\mathbf{r})$, uniformly distributed in the interval $(-U_0, U_0)$. We denote $H_0(\mathbf{k})$ as the lattice Hamiltonian for Eq. (1).

The self-energy defined by $(E_F - H_0 - \Sigma)^{-1} = \langle (E_F - H)^{-1}\rangle$, with $\langle\cdot\rangle$ the disorder average, is a 4×4 matrix which we decompose into Γ matrices: $\Sigma = \Sigma_0 + \Sigma_1\sigma_x\tau_z + \Sigma_2\sigma_y\tau_z + \Sigma_4\tau_x + \Sigma_5\sigma_z\tau_z$. Then the renormalized $\widetilde{m}_0$ and $\widetilde{\Delta}$ are given by

$$\widetilde{m}_0 = m_0 + \mathrm{Re}\Sigma_4, \quad \widetilde{\Delta} = \Delta + \mathrm{Re}\Sigma_5. \quad (2)$$

The self-consistent Born approximation (SCBA) is employed to capture the main feature of disorder [50], where Σ is given by the self-consistent equation

$$\Sigma = \frac{U_0^2}{3}\left(\frac{a}{2\pi}\right)^2 \int_{\mathrm{BZ}} d^2\mathbf{k} \frac{1}{\omega - H_0(\mathbf{k}) - \Sigma(\omega) + i0^+}. \quad (3)$$

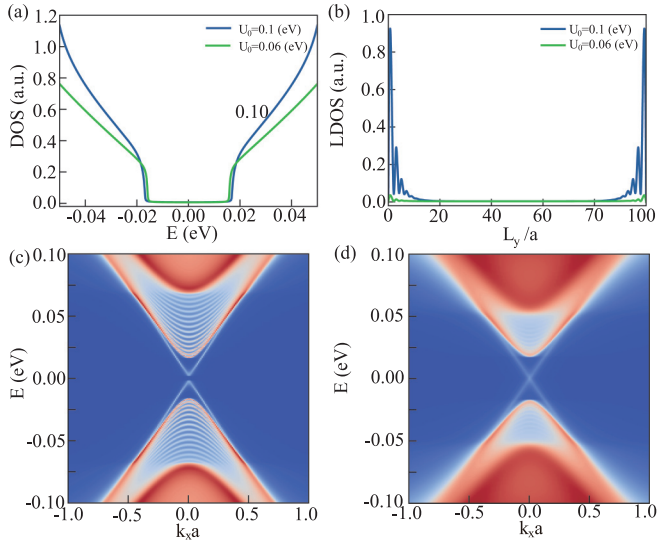

FIG. 2. (a) DOS of 2D bulk for typical U_0. (b) The real-space distribution for local DOS at $E = 0$ in (c) and (d). (c),(d) The edge spectral function $\mathcal{A}(k, \omega)$ within SCBA of disorder strength $U_0 = 0.06$ and $U_0 = 0.1$ eV, respectively. A cylinder geometry is adopted with periodic boundary condition along the x axis and open boundary condition in the y axis with width $L_y = 100a$. The lattice constant of the discretization $a = 2$ nm.

The self-energy is momentum independent, so there is no renormalization to v and m_1. The corrections to m_0 and Δ are approximately obtained as

$$\widetilde{m}_0 - m_0 = -\frac{U_0^2 a^2}{12\pi}\frac{1}{m_1}\ln\left|\frac{m_1^2\Pi^4}{m_0^2+\Delta^2-E_F^2}\right|, \tag{4a}$$

$$\widetilde{\Delta} - \Delta = \frac{U_0^2 a^2}{6\pi}\frac{\Delta\tanh^{-1}[\mathcal{Z}(k)]}{\sqrt{v^4+4v^2m_0m_1+4m_1^2\left(E_F^2-m_0^2\right)}}\Bigg|_0^{\Pi}, \tag{4b}$$

$$\mathcal{Z}(k) = \frac{v^2+2m_0m_1+2m_1^2k^2}{\sqrt{v^4+4v^2m_0m_1+4m_1^2\left(E_F^2-m_0^2\right)}}, \tag{4c}$$

where $\Pi = \pi/a$ is the ultraviolet cutoff in momentum. Here we only keep the most logarithmically divergent term in Eq. (4a). The sign of $\widetilde{m}_0$ and m_0 remains the same, as the correction to m_0 has the opposite sign to m_1. Then the system is always in the inverted region [51]. Similarly, the renormalized $\widetilde{\Delta}$ only decreases slightly. Therefore, the topological property of the 2D bulk remains unchanged due to disorder, which is evidenced in the density-of-state (DOS) calculation in Fig. 2(a).

To get information about the edge excitations in the disordered system, we further calculate the edge spectral function $\mathcal{A}(k, \omega)$ within SCBA in a cylinder geometry. The self-energy is $\Sigma(\omega, y) = (U_0^2/3)(a/2\pi)\int dk_x \mathcal{G}(\omega, k_x; y, y)$, with $\mathcal{G}(\omega, k_x; y, y)$ the Green's function on the cylinder, and the Dyson equation is $\mathcal{G}(k_x; y_1, y_0) = \int dy \mathcal{G}_0(k_x; y_1, y)\Sigma(y)\mathcal{G}(k_x; y, y_0) + \mathcal{G}_0(k_x; y_1, y_0)$. In a lattice $\int dy \to a\sum_i$, we have $\mathcal{G}(k_x)^{-1} = \mathcal{G}_0(k_x)^{-1} - \Sigma$. The spectral function $\mathcal{A}(k_x, \omega) = -(1/\pi)\mathrm{Im}\mathcal{G}^R(k_x, \omega)$ is plotted in Fig. 2 for different disorder strength U_0. We can see that the disorder broadens the quasiparticle spectral weight and reduces the edge gap when U_0 is relatively small. While U_0 exceeds a critical value U_c, the edge spectrum is gapless, as shown in Fig. 2(d), and such gapless state indeed resides at the sample boundary in Fig. 2(b). This explains the gapless edge state observed in this system by microwave impedance microscopy [42]. The edge gap closes earlier than the bulk gap as U increases (see Supplemental Material [49]). We point out that the gapless edge state here in the spectral function is essentially *different* from that in the topological Anderson insulator (TAI) [51–53]. In TAI, the gapless helical edge state is induced by disorder-driven band inversion, which is dissipationless and immune from backscattering as protected by Θ. Here in the disordered axion insulator film, the edge state is dissipative because Θ-breaking Δ induces backscattering. This is the main result of this paper.

The dissipative nature could be understood from the effective theory for the edge state with action,

$$\mathcal{S} = \int dtdx\psi^\dagger[\partial_t - iv\varrho_z\partial_x + \Delta\varrho_x + \mu(x)]\psi, \tag{5}$$

where $\mu(r)$ is the edge disorder potential with a zero mean. Via a nonlocal transformation $\psi = \mathcal{Q}(x)\widetilde{\psi}$, where $\mathcal{Q}(x) = \mathcal{P}\exp[-i\varrho_z\int_{-\infty}^{x} dx'\mu(x')/v]$, one can rewrite the action as

$$\mathcal{S} = \int dtdx\widetilde{\psi}^\dagger(\partial_t - iv\varrho_z\partial_x + \Delta\mathcal{Q}^\dagger\varrho_x\mathcal{Q})\psi, \tag{6}$$

where $\mathcal{P}$ stands for path ordering. The last term in Eq. (6) has long-range correlation from the random string phase factor $\mathcal{Q}$, which is a relevant perturbation and describes backscattering. This term is absent in the quantum Hall chiral edge states with $\nu = 2$ filling due to SU(2) symmetry [54,55]. Now we can see that the transformed action describes a gapless helical edge state with a backscattering term from random disorder.

IV. NUMERICS

The above analytic results can be corroborated numerically by using the package KWANT [56]. The resistance is calculated by the Landauer-Büttiker formalism with disorder-averaged transmission amplitude. The device geometry with the standard Hall bar is illustrated in Fig. 3(a). The two-terminal conductance G as a function of Fermi energy E_F is shown in Fig. 3(b). In the clean limit, G vanishes when E_F is in the edge gap and is finite, exhibiting oscillating behavior when E_F is in the Λ band, where the transmission resonance $G = 2e^2/h$ is consistent with the gapped helical edge state. For finite disorder, G is finite when E_F is even in the edge gap (of the clean limit) and gradually grows as E_F increases. The disappearance of conductance oscillation and $G < 2e^2/h$ when E_F is in the conducting edge band are the manifestation of the dissipative nature of the edge state. G as a function of disorder strength U_0 at $E_F = 0$ is plotted in Fig. 3(d). We can see G is finite only with moderate U_0. When $U_0 < U_c$, $G = 0$ due to the finite edge gap in the spectral function in Fig. 2, while G vanishes for strong U_0 due to the Anderson localization. Furthermore, the dissipative edge transport leads to monotonically decreasing G versus increasing device length L_x in Fig. 3(c).

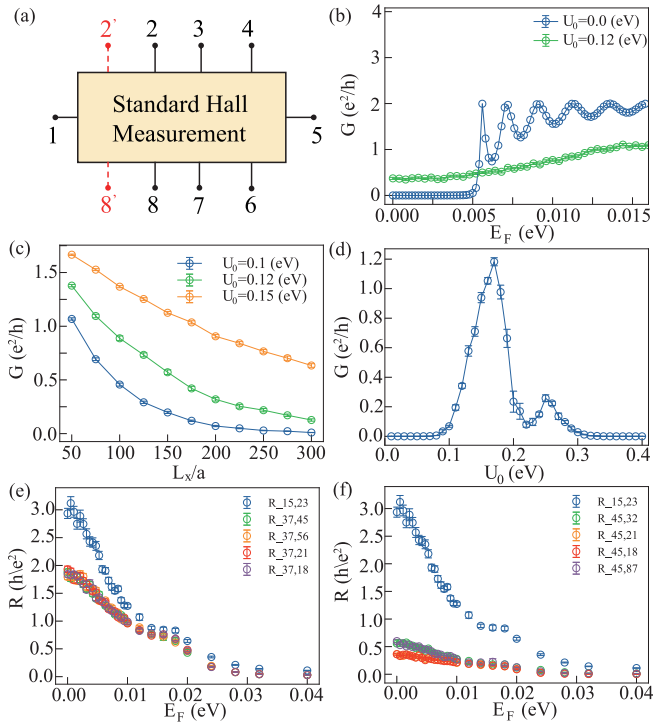

FIG. 3. (a) Schematic drawing of a Hall bar device. (b) The two-terminal longitudinal conductance G vs E_F with different U_0. (c) G vs L_x at $E_F = 0$ for different U_0, where $L_y = 100a$. (d) G vs U_0 at $E_F = 0$. The device size in (b) and (d) is $L_x \times L_y = 200a \times 100a$. (e),(f) The local and nonlocal resistance $R_{ij,kl}$ in an eight-terminal device as a function of E_F with $U_0 = 0.1$ eV. The device size in (e) and (f) is $L_x \times L_y = 300a \times 200a$. Each data point is a result of averaging over 500 disorder realizations.

The dissipative transport measured in the two terminals does not allow us to distinguish experimentally between helical edge channels and residual bulk conduction channels in a convincing manner. An unambiguous way to reveal the existence of dissipative helical edge state transport in the system is to use nonlocal electrical measurements. The edge states necessarily lead to nonlocal transport, and such nonlocal transport provides definitive evidence for the existence of chiral edge states in the quantum Hall effect [57,58]. The nonlocal resistance $R_{ij,kl}$ is plotted in Figs. 3(e) and 3(f), which is defined as the voltage between electrode k and l divided by the current flowing through electrode i and j, i.e., $R_{ij,kl} = V_{kl}/I_{ij}$. All of the nonlocal resistances are greater than the corresponding quantized value for the dissipationless gapless helical edge state in QSH, which further demonstrates that the edge transport is dissipative here. The nonlocal resistances decrease and finally vanish when E_F further goes into the bulk, which is different from the layer Hall effect [59]. Moreover, one interesting feature in Fig. 3(f) is that $R_{15,23} \approx 4R_{45,kl}$, which agrees with the recent transport experiment qualitatively [41]. We emphasize that the transmission amplitude and resistance in numerical simulation depend on the system size and position of the electrodes, which is the key feature for dissipative edge transport in this system.

V. EDGE TRANSPORT

We further propose a theory for the dissipative edge transport within the general Landauer-Büttiker formalism [57,58], where the current-voltage relationship is expressed as $I_i = (e^2/h)\sum_j (T_{ji}V_i - T_{ij}V_j)$, where V_i is the voltage on the ith electrode, I_i is the current flowing out of the ith electrode into the sample, and T_{ji} is the transmission probability from the ith to the jth electrode. There is no net current ($I_j = 0$) on a voltage lead or floating probe j, and the total current is conserved, namely, $\sum_i I_i = 0$. The current is zero when all the potentials are equal, implying the sum rules $\sum_i T_{ji} = \sum_i T_{ij}$.

For a standard Hall bar with $\mathcal{N}$ current and voltage leads [such as Fig. 3(a) with $\mathcal{N} = 8$], the transmission matrix elements for the dissipative helical state are given by $T_{i+1,i} = T_{i,i+1} = \kappa_i$ (from the disorder-averaged $\mathcal{I}\Theta$ symmetry) and others $= 0$ (here we identify $i = \mathcal{N} + 1$ with $i = 1$). These states are not protected from backscattering and the transmission from one electrode to the next is not perfect, implying $\kappa_i < 1$ [60], which is different from the dissipationless helical edge states in QSH where $\kappa_i = 1$ [61]. In general, κ_i become zero for an infinitely large sample because dissipation occurs once the phase coherence is destroyed in the metallic leads or the momentum is relaxed, $\kappa_i \sim e^{-\ell/l_m}$, where ℓ is the size between adjacent leads, and l_m is the mean free path which is 1/2 of the localization length for the 1D state [62]. For simplicity, we have assumed T_{ij} to be translational invariant, namely, $T_{i+1,i} = \kappa$ is i independent. The edge theory leads to the two-terminal conductance $G \sim \kappa e^2/h \propto e^{-L_x/l_m}$, which agrees with Fig. 3(c) quantitatively. Considering again the nonlocal transport as in Fig. 3(f), one finds that $R_{15,23} = h/2\kappa e^2$, $R_{45,kl} = h/8\kappa e^2$, and the relation $R_{15,23} = 4R_{45,kl}$. As the temperature increases, the nonlocal resistance reduces due to the contribution from bulk conduction by thermal activation, which is consistent with the experimental observations [41].

The effect of decoherence between two real leads can be modeled as an extra floating lead, in which dissipative gapless helical states interact with infinitely many low-energy degrees of freedom, completely losing their phase coherence [61]. κ is length dependent for the dissipative helical state in the axion insulator film, while it is length independent ($\kappa = 1$) for the dissipationless helical state in QSH. This leads to quite different transport signatures between these two helical states. For example, if we put extra pairs of floating probes [2′ and 8′ in Fig. 3(a)] in the standard two-terminal device with $L \gg l_m$,

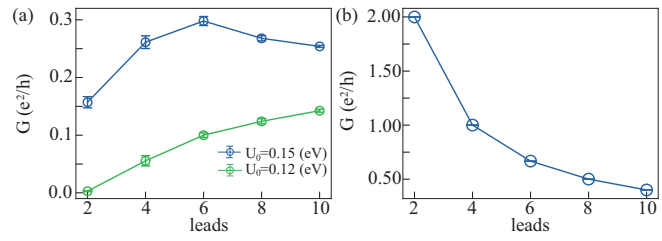

FIG. 4. The longitudinal conductance vs number of floating leads for (a) dissipative helical state in six-SL $MnBi_2Te_4$ with $U_0 = 0.12$ eV and $E_F = 0$, and (b) dissipationless helical state in QSH. The system size is $L_x \times L_y = 600a \times 100a$.

we can see that the longitudinal conductance increases (but not necessarily monotonically) as the number of floating leads increases for the dissipative helical state in Fig. 4(a) (see Supplemental Material [49]), which is just the opposite for QSH in Fig. 4(b). This is a rather sharp feature which is easy to implement in experiments.

VI. DISCUSSIONS

The dissipative gapless helical edge state from disorder in $MnBi_2Te_4$ films and its transport properties well explain the recent transport and image experiments [41,42]. The nonlocal resistance $R_{37,21}$ is greater than $R_{37,45}$, $R_{37,56}$, and $R_{37,18}$ in experiment [41] since κ is length dependent; one possible explanation is that the position of the electrodes is neither equally spaced nor perfectly aligned, which is common in experiments. Moreover, Eq. (1) also describes the low-energy physics in the FM-TI-FM heterostructure with $m_0 \approx 0$ [28], where the disorder will induce band inversion with a negative renormalized $\widetilde{m}_0$. However, the disorder strength is expected to be large and the exchange field is small in such a magnetically doped system [12]; thus the system is localized and should not have any gapless edge states. Finally, high magnetic field drives $MnBi_2Te_4$ even layer into a Chern insulator state with a full magnetization. The helical edge state from antiparallel magnetization of the axion insulator evolves into a chiral edge state from parallel magnetization of the Chern insulator, while other higher-energy helical states become quasihelical states with a larger edge gap due to stronger exchange field, and the transport is only determined by the dissipationless chiral edge channel.

In summary, disorder with moderate strength will dramatically modify the edge transport in axion insulator films, which is a generic phenomenon. The dissipative edge states could be probed by transport experiments with extra floating leads. Thinner films of the axion insulator such as four-SL $MnBi_2Te_4$ have a larger edge gap, as shown in Fig. 1(b); such gapped state may persist even in the presence of disorder and one can realize the long-sought TME effect in an axion insulator without any gapless states.

ACKNOWLEDGMENTS

We thank Jinsong Zhang and Eric Yue Ma for valuable discussions. This work is supported by the National Key Research Program of China under Grant No. 2019YFA0308404, the Natural Science Foundation of China through Grants No. 11774065 and No. 12174066, the Innovation Program for Quantum Science and Technology through Grant No. 2021ZD0302600, Shanghai Municipal Science and Technology Major Project under Grant No. 2019SHZDZX01, Science and Technology Commission of Shanghai Municipality under Grants No. 20JC1415900 and No. 23JC1400600, and the Natural Science Foundation of Shanghai under Grant No. 19ZR1471400.

Z.L. and D.Q. contributed equally to this work.

[1] D. J. Thouless, *Topological Quantum Numbers in Nonrealistic Physics* (World Scientific, Singapore, 1998).

[2] M. Z. Hasan and C. L. Kane, Colloquium: Topological insulators, Rev. Mod. Phys. **82**, 3045 (2010).

[3] X.-L. Qi and S.-C. Zhang, Topological insulators and superconductors, Rev. Mod. Phys. **83**, 1057 (2011).

[4] Y. Tokura, K. Yasuda, and A. Tsukazaki, Magnetic topological insulators, Nat. Rev. Phys. **1**, 126 (2019).

[5] X.-L. Qi, T. L. Hughes, and S.-C. Zhang, Topological field theory of time-reversal invariant insulators, Phys. Rev. B **78**, 195424 (2008).

[6] J. Wang and S.-C. Zhang, Topological states of condensed matter, Nat. Mater. **16**, 1062 (2017).

[7] C.-Z. Chang, J. Zhang, X. Feng, J. Shen, Z. Zhang, M. Guo, K. Li, Y. Ou, P. Wei, L.-L. Wang, Z.-Q. Ji, Y. Feng, S. Ji, X. Chen, J. Jia, X. Dai, Z. Fang, S.-C. Zhang, K. He, Y. Wang *et al.*, Experimental observation of the quantum anomalous Hall effect in a magnetic topological insulator, Science **340**, 167 (2013).

[8] J. G. Checkelsky, R. Yoshimi, A. Tsukazaki, K. S. Takahashi, Y. Kozuka, J. Falson, M. Kawasaki, and Y. Tokura, Trajectory of the anomalous Hall effect towards the quantized state in a ferromagnetic topological insulator, Nat. Phys. **10**, 731 (2014).

[9] X. Kou, S.-T. Guo, Y. Fan, L. Pan, M. Lang, Y. Jiang, Q. Shao, T. Nie, K. Murata, J. Tang, Y. Wang, L. He, T.-K. Lee, W.-L. Lee, and K. L. Wang, Scale-invariant quantum anomalous Hall effect in magnetic topological insulators beyond the two-dimensional limit, Phys. Rev. Lett. **113**, 137201 (2014).

[10] A. J. Bestwick, E. J. Fox, X. Kou, L. Pan, K. L. Wang, and D. Goldhaber-Gordon, Precise quantization of the anomalous Hall effect near zero magnetic field, Phys. Rev. Lett. **114**, 187201 (2015).

[11] C.-Z. Chang, W. Zhao, D. Y. Kim, H. Zhang, B. A. Assaf, D. Heiman, S.-C. Zhang, C. Liu, M. H. W. Chan, and J. S. Moodera, High-precision realization of robust quantum anomalous Hall state in a hard ferromagnetic topological insulator, Nat. Mater. **14**, 473 (2015).

[12] M. Mogi, R. Yoshimi, A. Tsukazaki, K. Yasuda, Y. Kozuka, K. S. Takahashi, M. Kawasaki, and Y. Tokura, Magnetic modulation doping in topological insulators toward higher-temperature quantum anomalous Hall effect, Appl. Phys. Lett. **107**, 182401 (2015).

[13] R. Watanabe, R. Yoshimi, M. Kawamura, M. Mogi, A. Tsukazaki, X. Z. Yu, K. Nakajima, K. S. Takahashi, M. Kawasaki, and Y. Tokura, Quantum anomalous Hall effect driven by magnetic proximity coupling in all-telluride based heterostructure, Appl. Phys. Lett. **115**, 102403 (2019).

[14] Y. Deng, Y. Yu, M. Z. Shi, Z. Guo, Z. Xu, J. Wang, X. H. Chen, and Y. Zhang, Quantum anomalous Hall effect in intrinsic magnetic topological insulator $MnBi_2Te_4$, Science **367**, 895 (2020).

[15] C.-X. Liu, X.-L. Qi, X. Dai, Z. Fang, and S.-C. Zhang, Quantum anomalous Hall effect in $Hg_{1-y}Mn_yTe$ quantum wells, Phys. Rev. Lett. **101**, 146802 (2008).

[16] R. Yu, W. Zhang, H.-J. Zhang, S.-C. Zhang, X. Dai, and Z. Fang, Quantized anomalous Hall effect

in magnetic topological insulators, Science **329**, 61 (2010).
[17] J. Wang, B. Lian, H. Zhang, Y. Xu, and S.-C. Zhang, Quantum anomalous Hall effect with higher plateaus, Phys. Rev. Lett. **111**, 136801 (2013).
[18] A. M. Essin, J. E. Moore, and D. Vanderbilt, Magnetoelectric polarizability and axion electrodynamics in crystalline insulators, Phys. Rev. Lett. **102**, 146805 (2009).
[19] S. Coh, D. Vanderbilt, A. Malashevich, and I. Souza, Chern-Simons orbital magnetoelectric coupling in generic insulators, Phys. Rev. B **83**, 085108 (2011).
[20] X. Wan, A. Vishwanath, and S. Y. Savrasov, Computational design of axion insulators based on 5*d* spinel compounds, Phys. Rev. Lett. **108**, 146601 (2012).
[21] A. M. Turner, Y. Zhang, R. S. K. Mong, and A. Vishwanath, Quantized response and topology of magnetic insulators with inversion symmetry, Phys. Rev. B **85**, 165120 (2012).
[22] N. Varnava and D. Vanderbilt, Surfaces of axion insulators, Phys. Rev. B **98**, 245117 (2018).
[23] A. Sekine and K. Nomura, Axion electrodynamics in topological materials, J. Appl. Phys. **129**, 141101 (2021).
[24] K. Nomura and N. Nagaosa, Surface-quantized anomalous Hall current and the magnetoelectric effect in magnetically disordered topological insulators, Phys. Rev. Lett. **106**, 166802 (2011).
[25] J. Wang, B. Lian, X.-L. Qi, and S.-C. Zhang, Quantized topological magnetoelectric effect of the zero-plateau quantum anomalous Hall state, Phys. Rev. B **92**, 081107(R) (2015).
[26] T. Morimoto, A. Furusaki, and N. Nagaosa, Topological magnetoelectric effects in thin films of topological insulators, Phys. Rev. B **92**, 085113 (2015).
[27] J. Wang, B. Lian, and S.-C. Zhang, Universal scaling of the quantum anomalous Hall plateau transition, Phys. Rev. B **89**, 085106 (2014).
[28] M. Mogi, M. Kawamura, R. Yoshimi, A. Tsukazaki, Y. Kozuka, N. Shirakawa, K. S. Takahashi, M. Kawasaki, and Y. Tokura, A magnetic heterostructure of topological insulators as a candidate for an axion insulator, Nat. Mater. **16**, 516 (2017).
[29] M. Mogi, M. Kawamura, A. Tsukazaki, R. Yoshimi, K. S. Takahashi, M. Kawasaki, and Y. Tokura, Tailoring tricolor structure of magnetic topological insulator for robust axion insulator, Sci. Adv. **3**, eaao1669 (2017).
[30] D. Xiao, J. Jiang, J.-H. Shin, W. Wang, F. Wang, Y.-F. Zhao, C. Liu, W. Wu, M. H. W. Chan, N. Samarth, and C.-Z. Chang, Realization of the axion insulator state in quantum anomalous Hall sandwich heterostructures, Phys. Rev. Lett. **120**, 056801 (2018).
[31] S. Grauer, K. M. Fijalkowski, S. Schreyeck, M. Winnerlein, K. Brunner, R. Thomale, C. Gould, and L. W. Molenkamp, Scaling of the quantum anomalous Hall effect as an indicator of axion electrodynamics, Phys. Rev. Lett. **118**, 246801 (2017).
[32] C. Liu, Y. Wang, H. Li, Y. Wu, Y. Li, J. Li, K. He, Y. Xu, J. Zhang, and Y. Wang, Robust axion insulator and Chern insulator phases in a two-dimensional antiferromagnetic topological insulator, Nat. Mater. **19**, 522 (2020).
[33] D. Zhang, M. Shi, T. Zhu, D. Xing, H. Zhang, and J. Wang, Topological axion states in the magnetic insulator $mnbi_2te_4$ with the quantized magnetoelectric effect, Phys. Rev. Lett. **122**, 206401 (2019).
[34] J. Li, Y. Li, S. Du, Z. Wang, B.-L. Gu, S.-C. Zhang, K. He, W. Duan, and Y. Xu, Intrinsic magnetic topological insulators in van der Waals layered $MnBi_2Te_4$-family materials, Sci. Adv. **5**, eaaw5685 (2019).
[35] M. M. Otrokov, I. P. Rusinov, M. Blanco-Rey, M. Hoffmann, A. Yu. Vyazovskaya, S. V. Eremeev, A. Ernst, P. M. Echenique, A. Arnau, and E. V. Chulkov, Unique thickness-dependent properties of the van der Waals interlayer antiferromagnet $MnBi_2Te_4$ films, Phys. Rev. Lett. **122**, 107202 (2019).
[36] R. Chen, S. Li, H.-P. Sun, Q. Liu, Y. Zhao, H.-Z. Lu, and X. C. Xie, Using nonlocal surface transport to identify the axion insulator, Phys. Rev. B **103**, L241409 (2021).
[37] H. Li, H. Jiang, C.-Z. Chen, and X. C. Xie, Critical behavior and universal signature of an axion insulator state, Phys. Rev. Lett. **126**, 156601 (2021).
[38] Z.-D. Song, B. Lian, R. Queiroz, R. Ilan, B. A. Bernevig, and A. Stern, Delocalization transition of a disordered axion insulator, Phys. Rev. Lett. **127**, 016602 (2021).
[39] Z. Liu and J. Wang, Anisotropic topological magnetoelectric effect in axion insulators, Phys. Rev. B **101**, 205130 (2020).
[40] M. Allen, Y. Cui, E. Yue Ma, M. Mogi, M. Kawamura, I. C. Fulga, D. Goldhaber-Gordon, Y. Tokura, and Z.-X. Shen, Visualization of an axion insulating state at the transition between 2 chiral quantum anomalous Hall states, Proc. Natl. Acad. Sci. USA **116**, 14511 (2019).
[41] Y. Li, C. Liu, Y. Wang, Z. Lian, S. Li, H. Li, Y. Wu, H.-Z. Lu, J. Zhang, and Y. Wang, Giant nonlocal edge conduction in the axion insulator state of $MnBi_2Te_4$, Sci. Bull. **68**, 1252 (2023).
[42] W. Lin, Y. Feng, Y. Wang, Z. Lian, H. Li, Y. Wu, C. Liu, Y. Wang, J. Zhang, Y. Wang, X. Zhou, and J. Shen, Direct visualization of edge state in even-layer $MnBi_2Te_4$ at zero magnetic field, Nat. Commun. **13**, 7714 (2022).
[43] R. S. K. Mong, A. M. Essin, and J. E. Moore, Antiferromagnetic topological insulators, Phys. Rev. B **81**, 245209 (2010).
[44] C.-X. Liu, H.-J. Zhang, B. Yan, X.-L. Qi, T. Frauenheim, X. Dai, Z. Fang, and S.-C. Zhang, Oscillatory crossover from two-dimensional to three-dimensional topological insulators, Phys. Rev. B **81**, 041307(R) (2010).
[45] H.-Z. Lu, W.-Y. Shan, W. Yao, Q. Niu, and S.-Q. Shen, Massive Dirac fermions and spin physics in an ultrathin film of topological insulator, Phys. Rev. B **81**, 115407 (2010).
[46] J. Zhang, Z. Liu, and J. Wang, In-plane magnetic-field-induced quantum anomalous Hall plateau transition, Phys. Rev. B **100**, 165117 (2019).
[47] H.-P. Sun, C. M. Wang, S.-B. Zhang, R. Chen, Y. Zhao, C. Liu, Q. Liu, C. Chen, H.-Z. Lu, and X. C. Xie, Analytical solution for the surface states of the antiferromagnetic topological insulator $mnbi_2te_4$, Phys. Rev. B **102**, 241406(R) (2020).
[48] B. A. Bernevig, T. L. Hughes, and S.-C. Zhang, Quantum spin Hall effect and topological phase transition in HgTe quantum wells, Science **314**, 1757 (2006).
[49] See Supplemental Material at http://link.aps.org/supplemental/10.1103/PhysRevB.108.245116 for technical details on first-principles calculations and tight-binding models, which includes Refs. [63–71].
[50] A. Altland and B. Simons, *Condensed Matter Field Theory* (Cambridge University Press, Cambridge, 2010).
[51] C. W. Groth, M. Wimmer, A. R. Akhmerov, J. Tworzydło, and C. W. J. Beenakker, Theory of the topological Anderson insulator, Phys. Rev. Lett. **103**, 196805 (2009).

[52] J. Li, R.-L. Chu, J. K. Jain, and S.-Q. Shen, Topological Anderson insulator, Phys. Rev. Lett. **102**, 136806 (2009).

[53] H. Jiang, L. Wang, Q.-F. Sun, and X. C. Xie, Numerical study of the topological Anderson insulator in HgTe/CdTe quantum wells, Phys. Rev. B **80**, 165316 (2009).

[54] C. L. Kane and M. P. A. Fisher, Edge-state transport, in *Perspectives in Quantum Hall Effects*, edited by S. D. Sarma and A. Pinczuk (Wiley-VCH Verlag GmbH, New York, 2007), pp. 109–159.

[55] T. Giamarchi, *Quantum Physics in One Dimension*, Vol. 121 (Clarendon, Oxford, 2003).

[56] C. W. Groth, M. Wimmer, A. R. Akhmerov, and X. Waintal, Kwant: A software package for quantum transport, New J. Phys. **16**, 063065 (2014).

[57] M. Büttiker, Four-terminal phase-coherent conductance, Phys. Rev. Lett. **57**, 1761 (1986).

[58] M. Büttiker, Absence of backscattering in the quantum Hall effect in multiprobe conductors, Phys. Rev. B **38**, 9375 (1988).

[59] A. Gao, Y.-F. Liu, C. Hu, J.-X. Qiu, C. Tzschaschel, B. Ghosh, S.-C. Ho, D. Berube, R. Chen, H. Sun, Z. Zhang, X.-Y. Zhang, Y.-X. Wang, N. Wang, Z. Huang, C. Felser, A. Agarwal, T. Ding, H.-J. Tien, A. Akey *et al.*, Layer Hall effect in a 2D topological axion antiferromagnet, Nature (London) **595**, 521 (2021).

[60] J. Wang, B. Lian, H. Zhang, and S.-C. Zhang, Anomalous edge transport in the quantum anomalous Hall state, Phys. Rev. Lett. **111**, 086803 (2013).

[61] A. Roth, C. Brüne, H. Buhmann, L. W. Molenkamp, J. Maciejko, X.-L. Qi, and S.-C. Zhang, Nonlocal transport in the quantum spin Hall state, Science **325**, 294 (2009).

[62] D. J. Thouless, Localization distance and mean free path in one-dimensional disordered systems, J. Phys. C: Solid State Phys. **6**, L49 (1973).

[63] P. W. Anderson, D. J. Thouless, E. Abrahams, and D. S. Fisher, New method for a scaling theory of localization, Phys. Rev. B **22**, 3519 (1980).

[64] A. Weiße, G. Wellein, A. Alvermann, and H. Fehske, The kernel polynomial method, Rev. Mod. Phys. **78**, 275 (2006).

[65] G. Kresse and J. Furthmüller, Efficient iterative schemes for *ab initio* total-energy calculations using a plane-wave basis set, Phys. Rev. B **54**, 11169 (1996).

[66] P. E. Blöchl, Projector augmented-wave method, Phys. Rev. B **50**, 17953 (1994).

[67] J. P. Perdew, K. Burke, and M. Ernzerhof, Generalized gradient approximation made simple, Phys. Rev. Lett. **77**, 3865 (1996).

[68] S. Grimme, J. Antony, S. Ehrlich, and H. Krieg, A consistent and accurate *ab initio* parametrization of density functional dispersion correction (DFT-d) for the 94 elements H-Pu, J. Chem. Phys. **132**, 154104 (2010).

[69] S. L. Dudarev, G. A. Botton, S. Y. Savrasov, C. J. Humphreys, and A. P. Sutton, Electron-energy-loss spectra and the structural stability of nickel oxide: An LSDA+U study, Phys. Rev. B **57**, 1505 (1998).

[70] A. A. Mostofi, J. R. Yates, Y.-S. Lee, I. Souza, D. Vanderbilt, and N. Marzari, Wannier90: A tool for obtaining maximally-localised Wannier functions, Comput. Phys. Commun. **178**, 685 (2008).

[71] QuanSheng Wu, ShengNan Zhang, H.-F. Song, M. Troyer, and A. A. Soluyanov, Wanniertools: An open-source software package for novel topological materials, Comput. Phys. Commun. **224**, 405 (2018).